Composites Communications 24 (2021) 100610

Contents lists available at ScienceDirect

Composites Communications

journal homepage: www.elsevier.com/locate/coco

# Polyaniline-decorated 3D carbon porous network with excellent electrolyte wettability and high energy density for supercapacitors

Siliang Liu [a], Kening Wan [c], Chao Zhang [a,*], Tianxi Liu [a,b,**]

[a] State Key Laboratory for Modification of Chemical Fibers and Polymer Materials, College of Materials Science and Engineering, Innovation Center for Textile Science and Technology, Donghua University, Shanghai, 201620, PR China

[b] Key Laboratory of Synthetic and Biological Colloids, Ministry of Education, School of Chemical and Material Engineering, Jiangnan University, Wuxi, 214122, PR China

[c] School of Engineering and Materials Science, Queen Mary University of London, Mile End Road, London, E14NS, United Kingdom

ARTICLE INFO

*Keywords:*
3D carbon network
Polyaniline
Electrolyte wettability
Supercapacitor electrode

ABSTRACT

The achievement of electrode materials with favorable electrolytic wettability is of significance for raising their electrochemical performance due to the occurring of electrostatic and pseudocapacitive processes at the interface. Herein, a polyaniline-decorated carbon nanofiber/nanosheet network (PANI@CNF/CNS) was prepared by in-situ polymerization of PANI on the surface of an interwoven carbon nanofiber/nanosheet network (CNF/CNS). Molten-salt pyrolysis of bacterial celluloses produced CNF/CNS hybrids, which were subsequently used as a 3D interwoven conductive network for the decoration of PANI. Benefiting from high conductivity of the hierarchical carbon network and fast ion transport within the PANI@CNF/CNS, an asymmetric supercapacitor using the PANI@CNF/CNS and CNF/CNS as cathode and anode materials, respectively, exhibited a high energy density of 65.3 W h $kg^{-1}$ at a power density of 800 W $kg^{-1}$ and an excellent cycling life of 98% retention after 5000 cycles at 10 A $g^{-1}$.

## 1. Introduction

With the rapid development of smart electronics, electric vehicles and portable digital devices, energy storage devices (e.g., lithium-ion batteries, fuel cells, supercapacitors) have been attracting increasing interest recently [1–3]. Among the numerous energy storage devices, supercapacitors, especially pseudocapacitors, have a promising prospect for realizing large-scale and high-performance energy-storage systems due to their unique features of lightweight, economical synthesis, environmental-friendly and high power density [4–8]. Compared with metal oxides/hydroxides and transition metal nitrides, conducting polymers of polyaniline (PANI) are great candidates as electrode materials for pseudocapacitors due to their easy synthesis, good environmental stability, and high theoretical capacitance [9]. However, the excellent electrochemical performance of pristine PANI is restricted by its poor cycling life, low rate capability, limited practical capacitance and high equivalent series resistance. This is because directly utilizing PANI as an electrode material suffers from challenges such as severe self-aggregation, high mass-transport resistance and large volumetric change during charge/discharge processes [10]. Besides, the reversible faradaic redox kinetics of PANI is hindered by its limited liquid-solid interface as well as the poor ion/electron mobility within the electrodes and at the electrode/electrolyte interface [11]. Therefore, the engineering of three-dimensional (3D) PANI architectures with fascinating conductivity and surface wettability is ungently needed to circumvent these demerits [12].

Recently, tremendous efforts have been devoted to achieving high energy storage of PANI electrode materials by incorporation of hierarchical carbon materials (e.g., carbon nanotubes, graphene, carbon aerogels) into nanostructured PANI (e.g., nanofiber, nanosheet, nanoflower) [3]. Among them, the preparation of hydrophilic PANI/hierarchical carbon composites provides the possibility for achieving efficient electrode materials with abundant electrochemically active sites, fast ion diffusion and good mechanical stability [13]. However, the architectural design and carbon substrate selection still impede the construction of hydrophilic PANI/hierarchical carbon conductive

* Corresponding author.
** Corresponding author. State Key Laboratory for Modification of Chemical Fibers and Polymer Materials, College of Materials Science and Engineering, Innovation Center for Textile Science and Technology, Donghua University, Shanghai, 201620, PR China.
*E-mail addresses:* czhang@dhu.edu.cn (C. Zhang), txliu@fudan.edu.cn (T. Liu).

https://doi.org/10.1016/j.coco.2020.100610
Received 29 October 2020; Received in revised form 23 December 2020; Accepted 23 December 2020
Available online 31 December 2020

networks [14]. The natural organisms provide enormous inspiration for the design of nanostructures with desirable properties. It is reported that the fish scales contain a superhydrophilic micropapillary and hierarchical rough structure, demonstrating superhydrophobicity in the air. This is because the hydrophilic chemical composition and strong capillary forces of fish scales improve the solution spreading capacity [15]. Therefore, the special structural features of fish scales provide feasible ideas for the construction of biomimetic PANI/hierarchical carbon architectures with excellent surface wettability [16]. Besides, the rational carbon frameworks with large surface area, tunable pore volume, high electrical conductivity and superior mechanical stiffness are also strictly required for the realization of high-energy-density PANI/hierarchical carbon electrode materials [11]. Compared with carbon nanotube, carbon nanobelt, carbon foam, etc., the carbon nanofiber (CNF) derived from bacterial cellulose (BC) is an attractive carbon framework due to its 3D conductive networks, availability and low cost [17]. Moreover, incorporation of carbon nanosheets (CNSs) into CNFs for consecutive CNF/CNS hybrid can further promote the mechanical strength, electrolyte contact area and ion/electron transport of carbon skeletons for hybridization with nanostructured PANI [2]. However, their practical application is dramatically limited by the long-duration and toxic synthesis routes [18]. Therefore, the synthesis of a hydrophilic PANI/hierarchical carbon network mimicking fish scales via an environmental-friendly and innovative method is a crucial challenge.

Herein, we proposed a simple and green approach for the preparation of an electrode material of fish scale-like hydrophilic PANI@CNF/CNS nanocomposites. Hierarchical CNF/CNS hybrids were first produced by the pyrolysis of BC in LiCl/KCl eutectics, and the CNF/CNS hybrids were subsequently employed as a 3D carbon framework for uniformly immobilizing a PANI nanorod array. The hierarchical porosity and microstructure of the CNF/CNS hybrids were tailored by varying the weight ratios of BC and molten salts. Molten salts can be easily removed and reused for subsequent synthesis, which is low-cost and environmental-friendly. The CNF/CNS hybrids exhibited a fast electron transport pathway, high specific area and well-balanced micro/mesoporous structure; meanwhile, the PANI@CNF/CNS networks demonstrated favorable wettability, enhanced ion diffusion in the electrodes-electrolyte interface and superior capacitance. As a result, the PANI@CNF/CNS electrodes performed a high specific capacitance and excellent rate capability. Moreover, an asymmetric supercapacitor with the PANI@CNF/CNS and CNF/CNS hybrid as positive and negative electrodes, respectively, exhibited an excellent energy density and a long cycling life. This finding thus developed a new strategy for the fabrication of high-performance electrode materials with excellent electrolyte wettability and high energy density for supercapacitors.

## 2. Results and discussion

Fig. 1a illustrates the fabrication process of the CNF/CNS hybrids and PANI@CNF/CNS. Briefly, freeze-dried BC squares were mixed with molten salts (LiCl/KCl: 0.45/0.55 by weight) and then pyrolyzed at 800 °C under a nitrogen atmosphere. After washed with 1 M HCl and water, the CNF/CNS hybrids were dried at 50 °C under vacuum overnight. Subsequently, the PANI@CNF/CNS networks were simply synthesized via in-situ growth of PANI nanorod arrays on the surface of the CNF/CNS hybrids.

Morphological evolutions of the CNF/CNS hybrids and PANI@CNF/CNS networks were characterized by transmission electron microscope (TEM) and scanning electron microscope (SEM). The CNF/CNS-1, CNF/CNS-2 and CNF/CNS-3 represent the pyrolyzed products with BC/molten salt feeding ratios of 1/20, 1/40 and 1/80, respectively. For comparison, the CNFs were fabricated by the same processes without molten salts, which showed the morphology of randomly oriented nanofibers with a diameter ranging from 20 to 50 nm (Fig. 1b–d). After adding molten salts into the precursor, the CNF/CNS-1 exhibited a highly interconnected and branched nanofiber network owing to the

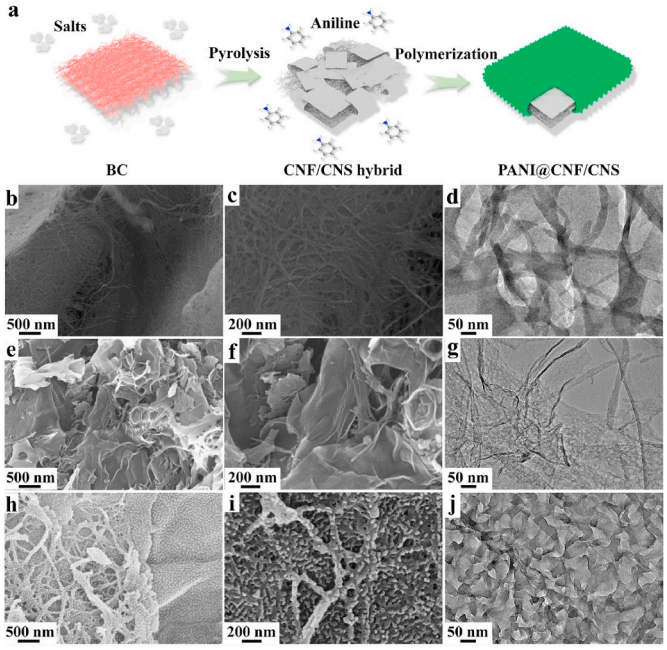


**Fig. 1.** (a) Schematic illustration of the preparation procedure of the CNF/CNS hybrid and PANI@CNF/CNS. SEM and TEM images of (b–d) CNFs, (e–g) CNF/CNS-2 and (h–j) PANI@CNS/CNF-2.

dissolution of outer cellulose chains in molten salts (Fig. S1a, b) [17]. With the increase of molten salt content in the precursor, the sheet-like CNS laminas were produced to construct the interwoven CNF/CNS hybrid for CNF/CNS-2 (Fig. 1e–g). Compared with CNF/CNS-1 and CNF/CNS-2, the morphology of CNF/CNS-3 showed less exposed CNFs and larger CNSs (Fig. S1c, d). The CNS exhibited a wrinkled nanosheet morphology without exposed CNFs, indicating the formation of ultrathin carbon architectures derived from BC (Fig. S2a, b). The increased molten salt content in pyrolysis facilitated the dissolution of BC and cycloaddition/elimination of carbonaceous derivatives, increasing the lateral size of CNS layers [19]. The formation of two-dimensional (2D) CNS nanostructures was possibly due to the extrusion of carbon from molten salts in a crystallization front line [20]. When the one-dimensional (1D) CNFs were embedded in the layers of 2D CNSs to construct the CNF/CNS hybrids, the CNFs served as junctions effectively prevented the self-aggregation of CNSs, and the CNSs assembled with CNFs to create 3D conductive pathways [21]. It was worth mentioning that the obtained carbon nanofibers showed similar diameter and length in both CNFs and CNF/CNS hybrids, which were directly carbonized by BC nanofibers due to the insufficient contact between molten salts and BC. Subsequently, the vertically aligned PANI nanorod arrays were chemically grown on the surface of CNF/CNS hybrids to construct hydrophilic PANI@CNF/CNS networks, mimicking the micro-nano scale hydrophilic protrusions on fish scales [22]. The length of PANI nanorod arrays was controlled by adding the various concentration of aniline while keeping the feeding content of CNF/CNS-2 constant. The resultant PANI@CNF/CNS networks are denoted as PANI@CNF/CNS-1, PANI@CNF/CNS-2 and PANI@CNF/CNS-3 with the concentration of aniline increasing from 20 to 80 mM. Fig. 1h–j showed the PANI nanorods were homogeneously deposited on the outer surface of both carbon nanofibers and carbon nanosheets for PANI@CNF/CNS-2. Besides, the hierarchical CNF/CNS skeleton was retained after the mechanical agitation, verifying the carbon nanofibers and carbon nanosheets were strongly conjoined together. Compared to the short and sparse PANI nanorods in PANI@CNF/CNS-1 (Fig. S3a, b) and the apparent aggregation of PANI in PANI@CNF/CNS-3 (Fig. S3c, d), the PANI@CNF/CNS-2 showed the morphology of vertically aligned PANI nanorod arrays with the average length of ~20 nm. The contents of PANI in each PANI@CNF/CNS were

calculated by comparing the weight of samples before and after growing the PANI. The solid content of PANI in PANI@CNF/CNS-1, PANI@CNF/CNS-2 and PANI@CNF/CNS-3 was calculated as 42.7, 65.6 and 79.1 wt%, respectively.

The crystalline structures of CNFs, CNF/CNS hybrids and PANI@CNF/CNS networks are characterized by XRD patterns (Fig. 2a). All the CNF/CNS hybrids and the neat CNFs revealed the two characteristic peaks at 26° and 43°, corresponding to the (002) and (100) planes of graphite carbon, respectively (Fig. S4a) [23]. The results suggested the carbon materials were successfully synthesized via the molten-salt pyrolysis of BC [12]. Compared with the CNF/CNS hybrids, the PANI@CNF/CNS networks exhibited 15°, 20.3°, and 25.4° patterns assigned to (011), (020), and (200) planes, respectively, which corresponded to the characteristic diffraction peaks of the neat PANI (Fig. S4b) [24,25]. Fig. 2b exhibits the Raman spectra of the CNFs, CNF/CNS hybrids and PANI@CNF/CNS networks. The two characteristic peaks at 1351 and 1578 $cm^{-1}$ for all CNF/CNS hybrids and the neat CNFs belonged to D and G bands (Fig. S5a). The D-band is related to the disordered crystalline structure in carbon materials, and the G-band attributes to the regular $sp^2$ carbon atoms in the graphitic area, and thus the intensity ratios of D and G band ($I_D/I_G$) refers to the disordered carbon content in the materials [19]. Compared with the neat CNFs (1.04), the $I_D/I_G$ ratios of CNF/CNS hybrids reduced from 1.01 (CNF/CNS-1) to 0.96 (CNF/CNS-3), indicating the disordered carbon structure gradually decreased with the increase of molten salts [26]. With the addition of PANI, the PANI@CNF/CNS networks performed the characteristic bands at 1260 $cm^{-1}$, 1587 $cm^{-1}$, 1470 $cm^{-1}$ and 1422 $cm^{-1}$, corresponding to the C–H bending and C═C stretching in the quinoid ring and benzenoid ring as well as C═N stretching vibration, respectively (Fig. S5b) [27,28]. This result confirms the hydrophilic PANI nanorod arrays have been anchored on the surface of the CNF/CNS skeleton to prepare the biomimetic hydrophilic structure [29].

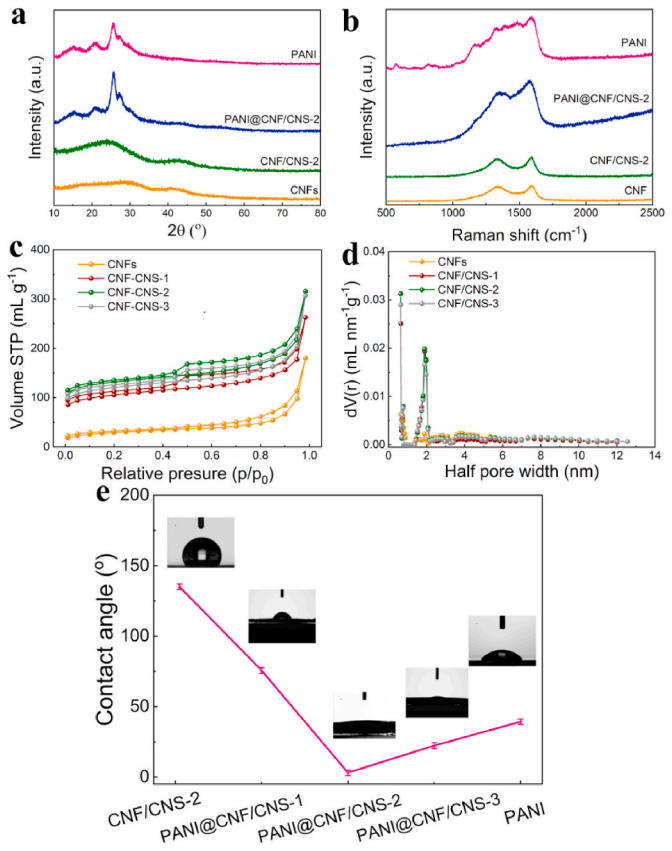


**Fig. 2.** (a) XRD patterns and (b) Raman spectra of CNFs, CNF/CNS-2, PANI@CNF/CNS-2 and PANI. (c) Nitrogen adsorption/desorption isotherms and (d) pore size distributions of CNFs and CNF/CNS hybrids. (e) Contact angles of neat PANI, CNF/CNS-2 and PANI@CNF/CNS with electrolytes.

The pore structures of CNF/CNS hybrids and CNFs are investigated by the nitrogen adsorption/desorption isotherms. Compared with the neat CNFs, the CNF/CNS hybrids exhibited the typical IV isotherms with a hysteresis loop when the relative pressure ranging from 0.4 to 1.0, indicating the existence of mesoporous structures (Fig. 2c) [30]. Besides, there existed a sharp slope in all CNF/CNS hybrids when relative pressure is below 0.1, suggesting the micropores have been introduced [31]. The pore size distributions of CNF/CNS hybrids and CNFs showed peaks varying from 1 to 18 nm, further verifying the formation of hierarchical micro/mesoporous structures (Fig. 2d). The hierarchically porous structure provided the possibility for increasing ion diffusions between CNF/CNS electrode materials and the electrolyte [30]. Investigated by Brunauer-Emmett-Teller (BET) method, the CNF/CNS-3 exhibited a higher specific surface area (452.1 $m^2$ $g^{-1}$) and pore volume (0.34 mL $g^{-1}$) compared with CNFs (91.8 $m^2$ $g^{-1}$, 0.16 mL $g^{-1}$), CNF/CNS-1 (375.4 $m^2$ $g^{-1}$, 0.28 mL $g^{-1}$) and CNF/CNS-2 (421.4 $m^2$ $g^{-1}$, 0.32 mL $g^{-1}$) in Table 1. The content of molten salts in precursor determined the specific surface and micro-mesopore volume of CNF/CNS hybrids. The percentage of CNS in each CNF/CNS hybrid was calculated by measuring the packing density of powder samples after mechanical oscillation. The packing densities of CNFs, CNF/CNS-1, CNF/CNS-2, CNF/CNS-3 and CNSs were calculated to be 0.34, 0.39, 0.46, 0.51 and 0.56 g $cm^{-3}$, respectively. Considering the well-distributed composition within the CNF/CNS hybrids and the packing density of CNFs and CNSs is constant, the percentages of CNSs in CNF/CNS-1, CNF/CNS-2 and CNF/CNS-3 were 22.7, 54.5 and 77.3 wt%, respectively, corresponding to the CNF/CNS hybrids with diverse specific surface area and micro-mesopore volume. This demonstrates that the porous structure of CNF/CNS hybrids can be simply tailored by varying the composition ratios of CNFs and CNSs. Based on the large specific surface area and interconnected micro/mesopores of CNF/CNS hybrids, the resultant PANI@CNF/CNS electrodes have great potential for enhancing rate capability and energy density as well as accommodating the volume changes during charge/discharge processes [31,32]. Electrical conductivities of neat CNFs and CNF/CNS hybrids were measured by four-probe measurements and summarized inTable S1. Profiting from the 3D conductive carbon framework and well-balanced micro/mesopores, the electrical conductivity of CNF/CNS-2 (14.7 S $m^{-1}$) is significantly higher than those of neat CNFs (2.1 S $m^{-1}$), CNF/CNS-1 (5.8 S $m^{-1}$) and CNF/CNS-3 (7.3 S $m^{-1}$). The uniform distribution of the CNFs between the CNS layers effectively prevented their self-aggregation and increased the charge transfer channels within the consecutive CNF/CNS hybrids [19].

The hydrophilicity of bionic PANI@CNF/CNS networks is further characterized by electrolyte contact angle measurement (Fig. 2e). The CNF/CNS-2 performed hydrophobic surfaces with a static electrolyte contact angle of 135.4° owing to its low-density and porous structure. In contrast, the PANI@CNF/CNS-2 shows hydrophilic surfaces with an electrolyte contact angle of 3.1°. This confirmed the adhesion ability and average surface energy of PANI@CNF/CNS-2 for electrolyte was dramatically promoted by the growth of PANI nanorod arrays onto the surface of the CNF/CNS-2 skeleton [33]. However, the contact angles of

**Table 1**
BET surface area and pore size distributions of the CNF/CNS hybrid and CNFs.

| Samples | $S_{BET}$ [$m^2$ $g^{-1}$] | Pore volume [mL $g^{-1}$] | Micropore volume [mL $g^{-1}$] | Mesopore volume [mL $g^{-1}$] |
|---|---|---|---|---|
| CNF/CNS-1 | 375.4 | 0.28 | 0.13 | 0.15 |
| CNF/CNS-2 | 421.4 | 0.32 | 0.15 | 0.17 |
| CNF/CNS-3 | 452.1 | 0.34 | 0.16 | 0.18 |
| CNFs | 91.8 | 0.16 | 0.03 | 0.13 |

PANI@CNF/CNS-1 and PANI@CNF/CNS-3 are 75.6° and 22.4°, which is attributed to the inhomogeneous deposition of PANI nanorods on carbon substrates. This superior electrolyte wettability of PANI@CNF/CNS-2 was not only due to the hydrophilicity of pristine PANI with a contact angle of 39.3°, but also ascribed to the fish scale-like PANI nanorod arrays, which probably enhanced the electrolyte spreading capacity in the electrode-electrolyte interfaces under the strong capillary forces [15,33,34]. Therefore, these superhydrophobic surfaces endow the resultant PANI@CNF/CNS-2 with increased permeation rate of hydrated ions and abundant electrochemically active sites [22,34].

The electrochemical performance of CNF/CNS hybrids and neat CNFs is evaluated by cyclic voltammetry (CV) curves (Fig. 3a). The electrode with a thickness of ~0.02 mm was coated on a graphite paper current collector (thickness: 0.02 mm) in an area of 1*1 $cm^2$. All samples showed approximately rectangle-shaped curves on behalf of their ideal double-layer capacitor performance [35,36]. The CV curve of CNF/CNS-2 showed the largest enclosed area among all the CNF/CNS hybrids and neat CNFs, suggesting the highest specific capacitance. Comparing the specific capacitance of the CNF/CNS hybrids and CNFs at different current densities from 1A $g^{-1}$ to 10A $g^{-1}$, the CNF/CNS-2 kept the highest specific capacitance at the same current density (Fig. 3b). In particular, the specific capacitance of CNF/CNS-2 was 308.8 F $g^{-1}$ at 1 A $g^{-1}$ with capacitance retention of 56.5% even at a high current density of 10 A $g^{-1}$, which was competitive to that of CNFs (100.3 F $g^{-1}$ with 61.8%), CNF/CNS-1 (200.4 F $g^{-1}$ with 63.8%) and CNF/CNS-3 (193.1 F $g^{-1}$ with 48.6%), respectively. The high specific capacitance and good rate capability of the CNF/CNS-2 electrode were attributed to its hierarchically micro/mesoporous carbon structure and interconnected conductive pathway, which decreased the resistance of electron/ion transport for a fast current-voltage response [17,18,37]. Electrochemical impedance spectroscopy (EIS) was used to measure the internal resistance and interfacial contact resistance of all the samples (Fig. 3c). The Nyquist plots of CNF/CNS hybrids and neat CNFs showed nearly straight lines in low-frequency regions, indicating the ideal electric double-layer capacitance behaviors [10]. The absence of the semicircle in high-frequency regions implied the fast ion diffusion and low charge-transfer resistance within CNF/CNS hybrids [38]. Compared with the CNF/CNS-2, the CNF/CNS-3 electrode stored a relatively low capacitance. This is because the CNS layers with an increased content among the CNF/CNS-3 were easily agglomerated into a compact assembled structure. The compact structure made the electrolytic ions difficult to diffuse into the interior parts of electrodes, leading to insufficient utilization of the intrinsic high surface area of the CNF/CNS-3 [39]. Besides, the lower electrical conductivity of CNF/CNS-3 (7.3 S $m^{-1}$) compared to CNF/CNS-2 (14.7 S $m^{-1}$) made the electron transfer inside the electrode not that efficient. Compared with the CNFs, CNF/CNS-1 and CNF/CNS-3, the CNF/CNS-2 exhibited relatively large surface area and balanced micro/mesopore distribution, which was demonstrated as an ideal conductive substrate for the uniform deposition of PANI nanorod arrays with more ion-accessible sites. Additionally, benefiting from its high mechanical stiffness, rapid electrolyte penetration and good electrical conductivity, the CNF/CNS-2 showed the highest specific capacitance and excellent rate performance among all CNF/CNS samples. The interconnected conductive CNF/CNS-2 framework greatly increased ultrafast charge/ion transfer and electroactive stability of the PANI@CNF/CNS [40]. Therefore, these merits of CNF/CNS-2 made it a promising substrate for the subsequent growth of PANI.

The CV curves of the bio-inspired superhydrophilic PANI@CNF/CNS networks and pristine PANI are shown in Fig. 3d. All the samples exhibited two pairs of redox peaks of PANI, suggesting the leucoemeraldine states of PANI were converted to emeraldine salt states and then to the pernigraniline states. Compared with other samples, PANI@CNF/CNS-2 showed a higher specific capacitance. For the PANI@CNF/CNS-2, the superior hydrophilicity of PANI nanorod arrays possibly increased the diffusion coefficient and shorten diffusion length of electrolyte in the electrode-electrolyte interfaces, and the 3D hierarchical CNF/CNS formworks provided an excellent conductivity [27,38]. Based on the galvanostatic charge-discharge curves, the specific capacitance of PANI@CNF/CNS and pristine PANI at different densities varying from 1A $g^{-1}$ to 10A $g^{-1}$ were calculated (Fig. 3e). The PANI@CNF/CNS-2 exhibited the highest specific capacitance of 810 F $g^{-1}$ at 1 A $g^{-1}$ compared with PANI@CNF/CNS-1 (381.8 F $g^{-1}$ at 1 A $g^{-1}$), PANI@CNF/CNS-3 (586 F $g^{-1}$ at 1 A $g^{-1}$) and PANI (260 F $g^{-1}$ at 1 A $g^{-1}$). The reduced capacitance of PANI@CNF/CNS-3 was because entangled PANI nanowires agglomerated together on the surface of CNF/CNS substrates and thus damaged its superhydrophobic architectures. When the current density reaches up to 10A $g^{-1}$,

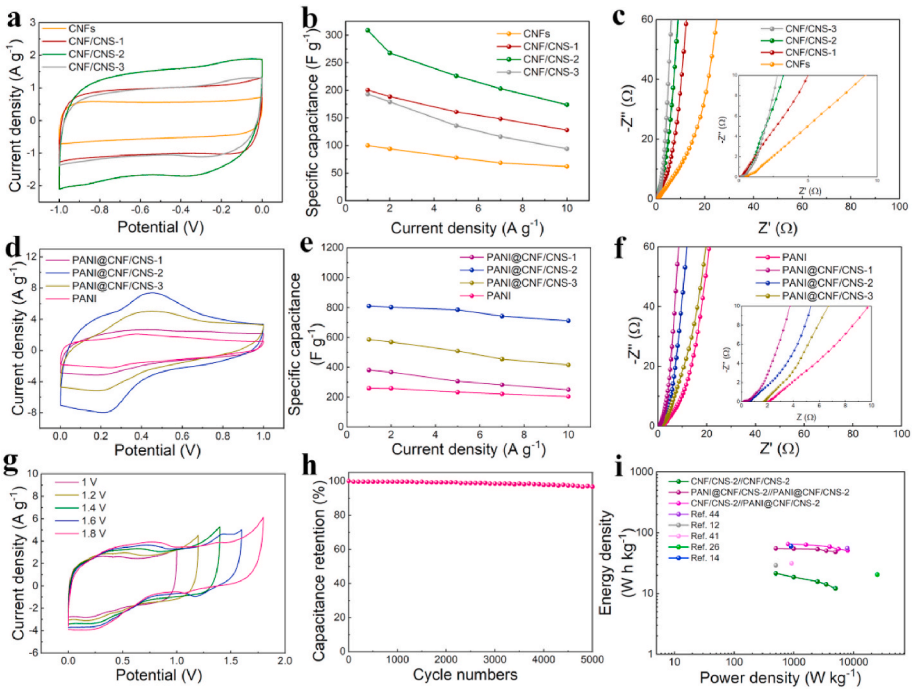


**Fig. 3.** (a) CV curves of CNF/CNS hybrids and CNFs at 10 mV $s^{-1}$. (b) Specific capacitances of CNF/CNS hybrids and CNFs at various current densities. (c) EIS curves of CNF/CNS hybrids and CNFs. (d) CV curves of PANI@CNF/CNS and PANI at 10 mV $s^{-1}$. (e) Specific capacitances of PANI@CNF/CNS and PANI at various current densities. (f) EIS curves of PANI@CNF/CNS and PANI. (g) CV curves of CNF/CNS-2//PANI@CNF/CNS-2 ASC device at various voltage windows. (h) Cycling performance of ASC device at 10 A $g^{-1}$. (i) Ragone plots of supercapacitors based on symmetric CNF/CNS-2, symmetric PANI@CNF/CNS-2 and asymmetric CNF/CNS-2//PANI@CNF/CNS-2 electrodes compared with other carbon/PANI composite electrodes in the literature.

PANI@CNF/CNS-2 still showed a higher specific capacitance of 712 F $g^{-1}$ than that of PANI@CNF/CNS-1 (250 F $g^{-1}$), PANI@CNF/CNS-3 (416 F $g^{-1}$) and the pristine PANI (204 F $g^{-1}$), respectively. The electrochemical reaction between the interfaces of electrode and electrolyte for PANI@CNF/CNS networks and pristine PANI was also studied by electrochemical impedance spectroscopy (EIS) in Fig. 3f. The PANI@CNF/CNS networks showed smaller semicircles and intercepts on the Z′ axis in the high-frequency region than pristine PANI, indicating their low charge transfer resistance ($R_{ct}$) and depressed equivalent series resistance (Rs) [41–43]. In the low-frequency part of the Nyquist plots, the slopes of PANI@CNF/CNS networks were much higher than that of the pristine PANI, corresponding to their efficient ion exchange and electron transfer at bionic electrode-electrolyte interfaces [44]. The key role to enhance the capacitive performance of the PANI@CNF/CNS was explained as follows: (i) The presence of consecutive CNF/CNS formwork acting as a highly conductive substrate to load PANI nanorod arrays with enhanced electrode/electrolyte interfacial areas; (ii) The CNF/CNS formwork with high mechanical stability acting as an elastic buffer effectively overcame the aggregation of PANI during cycling; (iii) The PANI@CNF/CNS network with fascinating surface wettability provided shortened pathways for infiltration of electrolytic ions, and the CNF/CNS formwork with hierarchically meso/microporous structure provided large ion reservoirs especially for fast insertion and extraction of ions. Therefore, the above-mentioned optimized nanostructures and synergistic effects between the PANI nanorod arrays and CNF/CNS formwork effectively endowed the resultant PANI@CNF/CNS network with excellent energy storage performance.

An asymmetric supercapacitor (ASC) device is further assembled by using PANI@CNF/CNS-2 as positive electrode materials and CNF/CNS-2 as negative electrode materials. The electrochemical performance of the as-fabricated ASC is evaluated in a two-electrode configuration. The operating cell voltage of the ASC was greatly enhanced due to different electrode-potential ranges of positive and negative electrode materials [12]. The CV curves of the ASC are measured at different operating potential windows from 0-0.8 V to 0–1.8 V (Fig. 3g). The ASC showed quasi-rectangular shaped curves even at an operating voltage of 1.6 V, exhibiting its good capacitive behavior with a wide potential window. When the voltage window reaches up to 1.8 V, the CV curves of the ASC became distorted due to electrochemical water splitting and decomposition of PANI [45]. The as-assembled ASC showed excellent long-term electrochemical stability with 98% capacitance retention after 5000 cycles at 10 A $g^{-1}$ (Fig. 3h). The Ragone plots of the as-assembled ASC device and the symmetric supercapacitors based on CNF/CNS-2 and PANI@CNF/CNS-2 were compared with recent ASC devices assembled by previously reported PANI/carbon composites (Fig. 3i). The resultant ASC device showed a high energy density of 65.3 W h $kg^{-1}$ at a power density of 800 W $kg^{-1}$, which is better than the symmetrical supercapacitor of CNF/CNS-2 (21.4 W h $kg^{-1}$ at 500 W $kg^{-1}$), PANI@CNF/CNS-2 (55.2 W h $kg^{-1}$ at 500 W $kg^{-1}$) as well as the other ASC devices in the literature [12,14,44,46]. The high energy density and long cycle life of our ACS are explained as follows: (i) the CNF/CNS formworks with hierarchically meso/microporous structure not only provides high electronic conductivity, but also serve as effective elastic buffers to accommodate the volumetric change during charge/discharge processes [33,34]. (ii) the superhydrophilic PANI@CNF/CNS networks have short diffusion paths for ion insertion and expulsion, which improves the pseudocapacitance of PANI [44]. Therefore, the facile electrolyte-electrode interfacial contact, fast electron transport and good interaction between carbon substrates and PANI coatings of electrode materials endow the as-assembled ACS with optimizing electrochemical performance.

## 3. Conclusion

In summary, an easily scalable and environmentally friendly strategy was demonstrated for the construction of a bio-inspired hydrophilic PANI@CNF/CNS. The hierarchical CNF/CNS hybrids were fabricated by simple molten-salt pyrolysis of BC and further used as a conductive carbon substrate for the deposition of PANI nanorod arrays. The resultant hydrophilic PANI@CNF/CNS networks showed rapid ion diffusion and increased electrode-electrolyte contact areas, and their CNF/CNS frameworks provided interconnected electron transport pathways and tunable micro/mesoporous ion diffusion channels. As a result, the ASC device assembled by CNF/CNS-2 and PANI@CNF/CNS-2 exhibited a great energy density of 65.3 W h $kg^{-1}$, a large power density of 8 kW $kg^{-1}$ and excellent cycling performance (only 2% capacitance loss after 5000 cycles). Therefore, this work offers a facile and renewable way to construct favorable ASC device for various practical applications.

## CRediT authorship contribution statement

**Siliang Liu:** Visualization, Investigation, Data curation, Writing - original draft. **Kening Wan:** Visualization, Investigation, Writing - review & editing. **Chao Zhang:** Conceptualization, Methodology, Supervision, Writing - review & editing. **Tianxi Liu:** Conceptualization, Supervision.

## Declaration of competing interest

The authors declare that they have no known competing financial interests or personal relationships that could have appeared to influence the work reported in this paper.

## Acknowledgements

We are grateful for the financial support from the National Natural Science Foundation of China (51773035), the Fundamental Research Funds for the Central Universities (CUSF-DH-D-2018004), and the Shanghai Scientific and Technological Innovation Project (18JC1410600).

## Appendix A. Supplementary data

Supplementary data to this chapter can be found online at https://doi.org/10.1016/j.coco.2020.100610.

## References

[1] Y. Huang, M. Zhu, Y. Huang, Z. Pei, H. Li, Z. Wang, Q. Xue, C. Zhi, Multifunctional energy storage and conversion devices, Adv. Mater. 28 (2016) 8344–8364.
[2] J. Azadmanjiri, V.K. Srivastava, P. Kumar, M. Nikzad, J. Wang, A. Yu, Two- and three-dimensional graphene-based hybrid composites for advanced energy storage and conversion devices, J. Mater. Chem. A 6 (2018) 702–734.
[3] K.C. Ho, L. Lin, A review of electrode materials based on core-shell nanostructures for electrochemical supercapacitors, J. Mater. Chem. A 7 (2019) 3516–3530.
[4] Q. Wang, J. Yan, Z. Fan, Carbon materials for high volumetric performance supercapacitors: design, progress, challenges and opportunities, Energy Environ. Sci. 9 (2016) 729–762.
[5] Z. Liu, L. Jiang, L. Sheng, Q. Zhou, T. Wei, B. Zhang, Z. Fan, Oxygen clusters distributed in graphene with "paddy land" structure: ultrahigh capacitance and rate performance for supercapacitors, Adv. Funct. Mater. 28 (2018) 1705258.
[6] L. Shao, J. Xu, J. Ma, B. Zhai, Y. Li, R. Xu, Z. Ma, G. Zhang, C. Wang, J. Qiu, Mxene/RGO composite aerogels with light and high-strength for supercapacitor electrode materials, Compos. Commun. 19 (2020) 108–113.
[7] J. Chen, Y. Huo, S. Li, Y. Huang, S. Lv, Host-guest complexes of β-cyclodextrin with methyl orange/methylene blue-derived multi-heteroatom doped carbon materials for supercapacitors, Compos. Commun. 16 (2019) 117–123.
[8] F. Lai, C. Yang, R. Lian, K. Chu, J. Qin, W. Zong, D. Rao, J. Hofkens, X. Lu, T. Liu, Three-phase boundary in cross-coupled micro-mesoporous networks enabling 3d-printed and ionogel-based quasi-solid-state micro-supercapacitors, Adv. Mater. 32 (2020) 2002474.
[9] J. Wu, Q. Zhang, J. Wang, X. Huang, H. Bai, A self-assembly route to porous polyaniline/reduced graphene oxide composite materials with molecular-level uniformity for high-performance supercapacitors, Energy Environ. Sci. 11 (2018) 1280–1286.
[10] D. Wu, W. Zhong, A new strategy for anchoring a functionalized graphene hydrogel in a carbon cloth network to support a lignosulfonate/polyaniline hydrogel as an integrated electrode for flexible high areal-capacitance supercapacitors, J. Mater. Chem. A 7 (2019) 5819–5830.

[11] D. Meng, J. Fan, J. Ma, S.-W. Du, J. Geng, The preparation and functional applications of carbon nanomaterial/conjugated polymer composites, Compos. Commun. 12 (2019) 64–73.
[12] S.K. Simotwo, V. Kalra, Polyaniline-carbon based binder-free asymmetric supercapacitor in neutral aqueous electrolyte, Electrochim. Acta 268 (2018) 131–138.
[13] J. Wang, L. Dong, C. Xu, D. Ren, X. Ma, F. Kang, Polymorphous supercapacitors constructed from flexible three-dimensional carbon network/polyaniline/MnO2 composite textiles, ACS Appl. Mater. Interfaces 10 (2018) 10851–10859.
[14] J. Shen, C. Yang, X. Li, G. Wang, High-performance asymmetric supercapacitor based on nanoarchitectured polyaniline/graphene/carbon nanotube and activated graphene electrodes, ACS Appl. Mater. Interfaces 5 (2013) 8467–8476.
[15] J. Yong, F. Chen, Q. Yang, D. Zhang, U. Farooq, G. Du, X. Hou, Bioinspired underwater superoleophobic surface with ultralow oil-adhesion achieved by femtosecond laser microfabrication, J. Mater. Chem. A 2 (2014) 8790–8795.
[16] Y. Zheng, H. Bai, Z. Huang, X. Tian, F.Q. Nie, Y. Zhao, J. Zhai, L. Jiang, Directional water collection on wetted spider silk, Nature 463 (2010) 640–643.
[17] S.F. Zhou, L.H. Zhou, Y.P. Zhang, J. Sun, J.L. Wen, Y. Yuan, Upgrading earth-abundant biomass into three-dimensional carbon materials for energy and environmental applications, J. Mater. Chem. A 7 (2019) 4217–4229.
[18] C. Xiong, Y. Zou, Z. Peng, W. Zhong, Synthesis of morphology-tunable electroactive biomass/graphene composites using metal ions for supercapacitors, Nanoscale 11 (2019) 7304–7316.
[19] S. Liu, J. Xu, J. Zhu, Y. Chang, H. Wang, Z. Liu, Y. Xu, C. Zhang, T. Liu, Leaf-inspired interwoven carbon nanosheet/nanotube homostructures for supercapacitors with high energy and power densities, J. Mater. Chem. A 5 (2017) 19997–20004.
[20] Q. Zheng, Z. Cai, Z. Ma, S. Gong, Cellulose nanofibril/reduced graphene oxide/carbon nanotube hybrid aerogels for highly flexible and all-solid-state supercapacitors, ACS Appl. Mater. Interfaces 7 (2015) 3263–3271.
[21] Z. Huang, H. Guo, C. Zhang, Assembly of 2D graphene sheets and 3D carbon nanospheres into flexible composite electrodes for high-performance supercapacitors, Compos. Commun. 12 (2019) 117–122.
[22] X. Yao, Y. Song, L. Jiang, Applications of bio-inspired special wettable surfaces, Adv. Mater. 23 (2011) 719–734.
[23] H. Guo, J. Zhou, Q. Li, Y. Li, W. Zong, J. Zhu, J. Xu, C. Zhang, T. Liu, Emerging dual-channel transition-metal-oxide quasiaerogels by self-embedded templating, Adv. Funct. Mater. 30 (2020) 2000024.
[24] J. Yan, T. Wei, Z. Fan, W. Qian, M. Zhang, X. Shen, F. Wei, Preparation of graphene nanosheet/carbon nanotube/polyaniline composite as electrode material for supercapacitors, J. Power Sources 195 (2010) 3041–3045.
[25] L. Li, Y. Zhang, H. Lu, Y. Wang, J. Xu, J. Zhu, C. Zhang, T. Liu, Cryopolymerization enables anisotropic polyaniline hybrid hydrogels with superelasticity and highly deformation-tolerant electrochemical energy storage, Nat. Commun. 11 (2020) 62.
[26] T. Purkait, G. Singh, N. Kamboj, M. Das, R.S. Dey, All-porous heterostructure of reduced graphene oxide-polypyrrole-nanoporous gold for a planar flexible supercapacitor showing outstanding volumetric capacitance and energy density, J. Mater. Chem. A 6 (2018) 22858–22869.
[27] Z. Huang, L. Li, Y. Wang, C. Zhang, T. Liu, Polyaniline/graphene nanocomposites towards high-performance supercapacitors: a review, Compos. Commun. 8 (2018) 83–91.
[28] J. Fu, J. Yun, S. Wu, L. Li, L. Yu, K.H. Kim, Architecturally robust graphene-encapsulated mxene Ti2CTx@polyaniline composite for high-performance pouch-type asymmetric supercapacitor, ACS Appl. Mater. Interfaces 10 (2018) 34212–34221.
[29] Y. Lin, H. Zhang, W. Deng, D. Zhang, N. Li, Q. Wu, C. He, In-situ growth of high-performance all-solid-state electrode for flexible supercapacitors based on carbon woven fabric/polyaniline/graphene composite, J. Power Sources 384 (2018) 278–286.
[30] L. Yan, D. Li, T. Yan, G. Chen, L. Shi, Z. An, D. Zhang, P. N, S-codoped hierarchically porous carbon spheres with well-balanced gravimetric/volumetric capacitance for supercapacitors, ACS Sustain. Chem. Eng. 6 (2018) 5265–5272.
[31] P. Du, Y. Dong, H. Kang, X. Yang, Q. Wang, J. Niu, S. Wang, P. Liu, Graphene-wrapped polyaniline nanowire array modified functionalized of carbon cloth for high-performance flexible solid state supercapacitor, ACS Sustain. Chem. Eng. 6 (2018) 14723–14733.
[32] H. Guo, Q. Feng, K. Xu, J. Xu, J. Zhu, C. Zhang, T. Liu, Self-templated conversion of metallogel into heterostructured TMP@carbon quasiaerogels boosting bifunctional electrocatalysis, Adv. Funct. Mater. 29 (2019) 1903660.
[33] H. Lv, X. Gao, Q. Xu, H. Liu, Y. Wang, Y. Xia, Carbon quantum dot-induced MnO2 nanowire formation and construction of a binder-free flexible membrane with excellent superhydrophilicity and enhanced supercapacitor performance, ACS Appl. Mater. Interfaces 9 (2017) 40394–40403.
[34] R. Soni, V. Kashyap, D. Nagaraju, S. Kurungot, Realizing high capacitance and rate capability in polyaniline by enhancing the electrochemical surface area through induction of superhydrophilicity, ACS Appl. Mater. Interfaces 10 (2018) 676–686.
[35] C. Gong, S. Sun, Y. Zhang, L. Sun, Z. Su, A. Wu, G. Wei, Hierarchical nanomaterials via biomolecular self-assembly and bioinspiration for energy and environmental applications, Nanoscale 11 (2019) 4147–4182.
[36] H. Huang, L. Peng, W. Fang, S. Cai, X. Chu, Y. Liu, W. Gao, Z. Xu, C. Gao, A polyimide-pyrolyzed carbon waste approach for the scalable and controlled electrochemical preparation of size-tunable graphene, Nanoscale 12 (2020) 11971–11978.
[37] J. Liang, C. Jiang, W. Wu, Toward fiber-, paper-, and foam-based flexible solid-state supercapacitors: electrode materials and device designs, Nanoscale 11 (2019) 7041–7061.
[38] A. Khosrozadeh, G. Singh, Q. Wang, G. Luo, M. Xing, Supercapacitor with extraordinary cycling stability and high rate from nano-architectured polyaniline/graphene on janus nanofibrous film with shape memory, J. Mater. Chem. A 6 (2018) 21064–21077.
[39] H. Lu, S. Liu, Y. Zhang, Y. Huang, C. Zhang, T. Liu, Nitrogen-doped carbon polyhedra nanopapers: an advanced binder-free electrode for high-performance supercapacitors, ACS Sustain. Chem. Eng. 7 (2019) 5240–5248.
[40] Y. Liu, L. Li, J. Zhu, J. Xu, S. Liu, Y. Wang, C. Zhang, T. Liu, A biomimetic setaria viridis-inspired electrode with polyaniline nanowire arrays aligned on MoO3@polypyrrole core–shell nanobelts, J. Mater. Chem. A 6 (2018) 13428–13437.
[41] F. Qin, X. Tian, Z. Guo, W. Shen, Asphaltene-based porous carbon nanosheet as electrode for supercapacitor, ACS Sustain. Chem. Eng. 6 (2018) 15708–15719.
[42] Y. Wang, M. Tebyetekerwa, Y. Liu, M. Wang, J. Zhu, J. Xu, C. Zhang, T. Liu, Extremely stretchable and healable ionic conductive hydrogels fabricated by surface competitive coordination for human-motion detection, Chem. Eng. J. (2021), https://doi.org/10.1016/j.cej.2020.127637.
[43] Y. Zheng, H. Song, S. Chen, X. Yu, J. Zhu, J. Xu, K.A.I. Zhang, C. Zhang, T. Liu, Metal-free multi-heteroatom-doped carbon bifunctional electrocatalysts derived from a covalent triazine polymer, Small 16 (2020) 2004342.
[44] V. Sahu, R.B. Marichi, G. Singh, R.K. Sharma, Hierarchical polyaniline spikes over vegetable oil derived carbon aerogel for solid-state symmetric/asymmetric supercapacitor, Electrochim. Acta 240 (2017) 146–154.
[45] J. Park, Y.E. Yoo, L.Q. Mai, W. Kim, Rational design of a redox-active nonaqueous electrolyte for a high-energy-density supercapacitor based on carbon nanotubes, ACS Sustain. Chem. Eng. 7 (2019) 7728–7735.
[46] P. Bandyopadhyay, T. Kuila, J. Balamurugan, T.T. Nguyen, N.H. Kim, J.H. Lee, Facile synthesis of novel sulfonated polyaniline functionalized graphene using m-aminobenzene sulfonic acid for asymmetric supercapacitor application, Chem. Eng. J. 308 (2017) 1174–1184.